

# Nanocrystalline Fe–C alloys produced by ball milling of iron and graphite

Y.Z. Chen<sup>a,b</sup>, A. Herz<sup>b,d</sup>, Y.J. Li<sup>b,c</sup>, C. Borchers<sup>b,\*</sup>, P. Choi<sup>c</sup>, D. Raabe<sup>c</sup>,  
R. Kirchheim<sup>b,c,e</sup>

<sup>a</sup> State Key Laboratory of Solidification Processing, Northwestern Polytechnical University, 710072 Xi'an, People's Republic of China

<sup>b</sup> Institut für Materialphysik, Universität Göttingen, 37077 Göttingen, Germany

<sup>c</sup> Max-Planck Institut für Eisenforschung GmbH, Department for Microstructure Physics, Max-Planck-Str.1, 40237 Düsseldorf, Germany

<sup>d</sup> Department of Materials for Electronics, Institute of Materials Engineering and Institute of Micro- and Nanotechnologies MacroNano<sup>®</sup>,  
Ilmenau University of Technology, 98684 Ilmenau, Germany

<sup>e</sup> International Institute for Carbon-Neutral Energy Research (WPI-I2CNER), Kyushu University, Japan

Received 19 December 2012; accepted 4 February 2013

Available online 16 March 2013

## Abstract

A series of nanocrystalline Fe–C alloys with different carbon concentrations ( $x_{tot}$ ) up to 19.4 at.% (4.90 wt.%) are prepared by ball milling. The microstructures of these alloys are characterized by transmission electron microscopy and X-ray diffraction, and partitioning of carbon between grain boundaries and grain interiors is determined by atom probe tomography. It is found that the segregation of carbon to grain boundaries of  $\alpha$ -ferrite can significantly reduce its grain size to a few nanometers. When the grain boundaries of ferrite are saturated with carbon, a metastable thermodynamic equilibrium between the matrix and the grain boundaries is approached, inducing a decreasing grain size with increasing  $x_{tot}$ . Eventually the size reaches a lower limit of about 6 nm in alloys with  $x_{tot} > 6.19$  at.% (1.40 wt.%); a further increase in  $x_{tot}$  leads to the precipitation of carbon as Fe<sub>3</sub>C. The observed presence of an amorphous structure in 19.4 at.% C (4.90 wt.%) alloy is ascribed to a deformation-driven amorphization of Fe<sub>3</sub>C by severe plastic deformation. By measuring the temperature dependence of the grain size for an alloy with 1.77 at.% C additional evidence is provided for a metastable equilibrium reached in the nanocrystalline alloy.

© 2013 Acta Materialia Inc. Published by Elsevier Ltd. All rights reserved.

**Keywords:** Thermodynamics; Fe–C alloy; Nanocrystalline materials; Segregation; Mechanical alloying

## 1. Introduction

Nanocrystalline materials have great potential in a variety of applications. However, due to the extremely high density of grain boundaries, many nanocrystalline materials suffer from microstructural instability. Therefore, it is difficult to achieve a thermally stable microstructure on the nanometer scale [1], a deficiency that strongly limits the application of these materials. A strategy to overcome

this limitation is to reduce the grain boundary energy by solute segregation and thus diminish the driving force for grain growth. The reduction of interfacial energy by solute segregation was quantitatively described by Gibbs [2] by his adsorption isotherm:

$$d\gamma = -\Gamma d\mu_A, \quad (1)$$

where  $\gamma$  is the interface or grain boundary energy,  $\Gamma$  is the excess solute at the boundary and  $\mu_A$  is the chemical potential of the solute A. Atoms of type A segregating to grain boundaries lead to a positive excess and thus reduce the grain boundary energy.

\* Corresponding author. Tel.: +49 551395584; fax: +49 551395012.

E-mail address: [chris@ump.gwdg.de](mailto:chris@ump.gwdg.de) (C. Borchers).

The concept of suppressing grain growth in nanocrystalline alloys by applying Gibbs' relation was first suggested by Birringer [3] and then quantitatively treated by Weissmüller [4,5]. The latter has shown that in the framework of thermodynamics a metastable equilibrium is attained in a closed system if the grain boundary energy is reduced to zero. For grain boundaries saturated with solute the following relation was derived by Weissmüller [4,5]:

$$\gamma = \gamma_o - \Gamma_{sat}(\Delta H_{seg} + RT \ln x_{gi}), \quad (2)$$

where  $\gamma_o$  is the energy of the pure grain boundary ( $\Gamma = 0$ ),  $\Gamma_{sat}$  is the excess solute for the boundary saturated with A,  $\Delta H_{seg}$  is the segregation energy of A (defined as positive for segregating species) and  $x_{gi}$  is the molar ratio of A within the grain interior. In order to reduce  $\gamma$  to a large fraction of  $\gamma_o$  both  $\Delta H_{seg}$  and  $x_{gi}$  have to be large because  $\Gamma_{sat}$  is expected to be of the order of one monolayer. Using reasonable figures for the quantities in Eq. (2) Weissmüller has shown that  $\gamma$  may become zero. However, it was also shown by one of the authors [6] that  $\gamma = 0$  may not be reached, because the two quantities in brackets might depend on each other. As proposed by Hondros et al. [7] the solubility of A (the upper value of  $x_A$ ) is related to the segregation enrichment factor (a measure of  $\Delta H_{seg}$ ). Thus oversaturation of A within the grains may be required to attain a value of  $\gamma = 0$  according to Eq. (2) [6]. In a generalization of Gibbs treatment [8,9] it was also shown that Eq. (1) is also valid for other discontinuities or defects such as vacancies, dislocations etc., and the term defactants was coined. Defactants segregate to defects and reduce their formation energy in the same way that surfactants segregate to surfaces reducing surface energies. In this context it was also shown [8] that Eq. (2) is a special case of Eq. (1) (see Appendix A) and that in open systems for  $\gamma < 0$  the attainment of metastable equilibrium with  $\gamma = 0$  requires that the derivative  $d\gamma/da$  is positive [10].

Since the pioneering work of Weissmüller [4,5] it has been shown in many studies [11–22] that nanocrystalline alloys can be stabilized by grain boundary segregation. Whether the stabilization was achieved by kinetic barriers or by reaching the equilibrium with  $\gamma = 0$  often remained an open question. Evidence for thermodynamic stabilization is provided by showing thermal stability of the nanocrystalline structure in the presence of segregating solutes, i.e. showing that  $\gamma$  as the driving force for grain growth is suppressed. Another approach for proving  $\gamma = 0$  is measuring the total solute concentration,  $c_{tot}$  (in mole m<sup>-3</sup>) and its partitioning between grain interior,  $c_{gi}$  and grain boundaries,  $c_{gb}$ . Solute conservation requires:

$$c_{tot} = c_{gi} + \frac{a\Gamma}{V}, \quad (3)$$

where  $a$  is the total grain boundary area,  $\Gamma$  the excess solute at these boundaries and  $V$  is the sample volume. For grains of cubic or spherical shape with a grain diameter,  $d$ , Eq. (3) becomes [4,17]:

$$c_{tot} = c_{gi} + \frac{3\Gamma}{d}. \quad (4)$$

Eqs. (3) and (4) are valid independent of the value of  $\gamma$ . However, for  $\gamma = 0$  Eq. (2) requires that  $c_{gi}$  is independent of the grain size  $d$ , reaching the constant value  $c_{gi}^o$ . Under these conditions the excess should have reached saturation and Eq. (4) takes the special form:

$$c_{tot} = c_{gi}^o + \frac{3\Gamma_{sat}}{d}. \quad (5)$$

Thus a hyperbolic relation between grain diameter and total solute concentration should exist for  $\gamma = 0$  as predicted [17,18,23] and experimentally proven [17,18]. Atom probe tomography (APT) is especially suited to measure both  $c_{gi}^o$  and  $\Gamma_{sat}$  as done for phosphorous in nanocrystalline nickel [17] and cobalt [18]. If the equilibrium values of  $c_{gi}^o$  and  $\Gamma_{sat}$  are known, a direct comparison of Eq. (5) with experimental results for  $d$  and  $c_{tot}$  becomes possible. Metastable thermodynamic equilibrium with the chemical potentials of solute atoms being the same in grain boundaries and the grain interior is possibly not yet established after preparation of nanocrystalline alloys but may require a moderate annealing treatment [17].

In the present study APT is used for nanocrystalline Fe–C alloys prepared by ball milling of iron and graphite. The grain size of the mechanically alloyed samples was determined by both dark-field transmission electron microscopy (TEM) and X-ray diffraction (XRD). Compared to the previous work by Hono et al. [24,25] the total carbon concentration was varied over a large range and a much larger number of grain boundaries was measured, because a local electrode atom probe (LEAP) was used to analyze a large volume, allowing fast data acquisition and high mass resolution [26–29]. Experimental data are evaluated on the basis of Eq. (5), in order to check whether equilibrium with  $\gamma = 0$  is attained. In addition, for one of the Fe–C alloys the temperature dependence of the average grain size was determined and compared with a new equation derived from Eqs. (2) and (5).

Unlike the thermodynamic approach, grain refinement induced by carbon addition is explained as promotion of dislocation multiplication and retardation of dynamic recovery by carbon during the ball-milling process [30]. It has already been shown by APT in previous studies that carbon atoms in ball-milled nanocrystalline Fe–C alloys exhibit pronounced segregation to grain boundaries of nanocrystalline ferrite [25,31]. However no quantitative comparison of experimental results with the theoretical predictions displayed in Eqs. (2) and (5) has been performed. This is done in the present work where the total carbon concentration and temperature were systematically varied.

It is interesting to note that the two equilibrium phases graphite and iron, used in this study and by Hono et al. as starting materials [24,25], should not intermix at room temperature according to the phase diagram. However, the external forces applied during ball milling drive the system

to a non-equilibrium state with carbon atoms sitting mostly at grain boundaries. A similar final nanocrystalline state can be obtained by using a pearlitic steel as starting material for superplastic deformation [30].

## 2. Experimental

### 2.1. Materials

Nanocrystalline Fe–C alloys with variable carbon concentrations labeled as alloys A, B, C, D, E, F and G in Table 1 were prepared by ball milling iron powder (99.99% purity) mixed with different amounts of graphite powder (99.99% purity). The ball-milling experiments were carried out with a Fritsch planetary mill Pulverisette 6 classic line including the Safe-Lock clamping system. The grinding bowl and grinding balls were made of zirconium dioxide. The ball to powder weight ratio was 10:1 (powders were handled in an argon glovebox to avoid contamination with oxygen). Ball milling of each powder mixture was conducted in an argon atmosphere for 100 h. In order to separate graphite not alloyed with iron the powders were immersed after ball milling into diiodomethane ( $\text{CH}_2\text{I}_2$ ) which has a higher density ( $3.325 \text{ g cm}^{-3}$ ) than graphite ( $2.09\text{--}2.23 \text{ g cm}^{-3}$ ) but a lower one than iron ( $7.874 \text{ g cm}^{-3}$ ). After stirring, the unalloyed graphite powders floated onto the surface of  $\text{CH}_2\text{I}_2$  while the Fe–C powders sank down to the bottom. Afterwards, the powders separated in  $\text{CH}_2\text{I}_2$  were cleaned in ethanol at least three times and dried in the fume hood at room temperature. The carbon concentrations  $c_{\text{tot}}$  of the cleaned powders were measured using a carbon analyzer (G4 Icarus CS HF, Bruker AXS), and are listed in Table 1. To investigate the changes of microstructure and distribution of carbon at higher temperatures, annealing treatments were performed in a high-vacuum furnace ( $\sim 10^{-5}$  mbar) and subsequently cooled down to room temperature within the furnace.

### 2.2. Characterization techniques

Microstructures of the powders were characterized by means of TEM and XRD. TEM specimens were prepared with a focused ion beam (FIB) FEI Nova 600 Nano Lab and were investigated in a Philips CM 30 TEM operated at an acceleration voltage of 300 kV. XRD measurements were obtained with a Philips X'pert MRD diffractometer using  $\text{Co } K_\alpha$  radiation ( $\lambda_{\text{Co}\alpha} = 0.178897 \text{ nm}$ ). Step size and counting time per step are  $0.02^\circ$  and 20 s, respectively. Calibration of the XRD results was done with a standard Si sample. The grain sizes of the powders were determined by analyzing TEM dark-field images and by X-ray line profile analysis (XLPA) [32–34]. The current XLPA was performed by means of the extended convolution multiple whole-profile (eCMWP) procedures [32–34] which is more elaborate than a simple Williamson–Hall analysis and yields more reliable results for the grain sizes and dislocation densities of the powders. The physical parameters used

Table 1

Fraction of graphite in the mixed powders and analyzed total carbon concentration  $c_{\text{tot}}$  of the ball-milled Fe–C alloys labelled A–G. Whether the samples were characterized by either XRD or TEM is marked in the last two lines.

	A	B	C	D	E	F	G
Graphite (at.%)	0.93	1.84	3.76	7.05	13.37	17.33	25
$x_{\text{tot}}$ (at.%)	0.93	1.77	3.27	6.19	13.34	14.21	19.4
$x_{\text{tot}}$ (wt.%)	0.20	0.38	0.72	1.40	3.19	3.43	4.90
$c_{\text{tot}}$ (mole $\text{m}^{-3}$ )	1300	2500	4600	8700	18800	20,000	27,400
XRD	Yes	Yes	Yes	Yes			
TEM		Yes	Yes		Yes	Yes	Yes

in eCMWP fitting are Burgers vector  $b = 0.248 \text{ nm}$  and average dislocation contrast factor  $C_{h00} = 0.256$  [35]. The distribution of grain sizes is assumed to be log-normal, i.e.  $f(d) = [1/(2\pi)^{1/2}\sigma](1/d) \exp\{-[\ln(d/m)]^2/2\sigma^2\}$  with  $d$  the grain size,  $\sigma^2$  the variance and  $m$  the median [32], which is ascertained by TEM analyses. According to Ref. [36], the area weight of  $d$  can be expressed as  $d_{\text{area}}^{\text{XLP}} = m \exp(2.5\sigma^2)$ .

In order to determine the lattice parameters of the powders, the positions of the Bragg peaks were obtained by fitting the measured XRD profiles with a pseudo-Voigt function with a Lorentzian factor of 0.5. Carbon concentrations in ferrite grains  $c_{\text{gi}}$  were determined via the lattice parameters using the equation  $x_{\text{gi}} = (a - a_0)/[(8.4 \pm 0.8) \times 10^{-3}]$  with  $a$  the measured lattice parameter of ferrite, and  $a_0 = (2.8664 \pm 0.0001) \text{ \AA}$  the lattice constant of pure iron [37]. Excess carbon in the grain boundaries was then calculated using the measured grain size and Eq. (4). It should be noted that there are some factors which may influence the measurements of the lattice parameters of ferrite. Upon ball milling, the materials are severely deformed. Since the temperature during the ball milling is relatively low (below 323 K in this work), a large number of vacancies might be produced, which could cause contraction of the lattice of ferrite leading to uncertainties in the evaluations of the carbon concentrations.

A local electrode atom probe (LEAP 3000X HR, Cameca Instruments) was employed for quantitative analyses of the carbon concentration at grain boundaries and grain interiors. The measurements were performed in voltage mode at 70 K under an ultra-high vacuum of  $8 \times 10^{-9} \text{ Pa}$ . The pulse fraction was 15%. The pulse repetition rate was 200 kHz at a detection rate of 0.005 atoms per pulse. The reconstruction of the atom probe data was done using standard parameters for iron. The final tip radii after APT measurements were also taken into account. Carbon peaks in the mass spectra were identified as  $\text{C}^{++}$  at 6 Da and 6.5 Da,  $\text{C}^+$  at 12 Da and 13 Da,  $\text{C}_3^{++}$  at 18 Da and 18.5 Da,  $\text{C}_2^+$  at 24 Da and 25 Da,  $\text{C}_4^{++}$  at 24.5 and  $\text{C}_3^+$  at 36 Da. The quantitative carbon distributions in grain interiors and at grain boundaries are analyzed for the individual subvolumes as illustrated in Fig. 1. An isoconcentration surface (in green) at 1.5 at.% C is shown in Fig. 1a to quantitatively distinguish grain boundaries from grain interiors, which are displayed in Fig. 1b and c, respectively. This method yields relatively accurate concentration values, because for each region of interest its

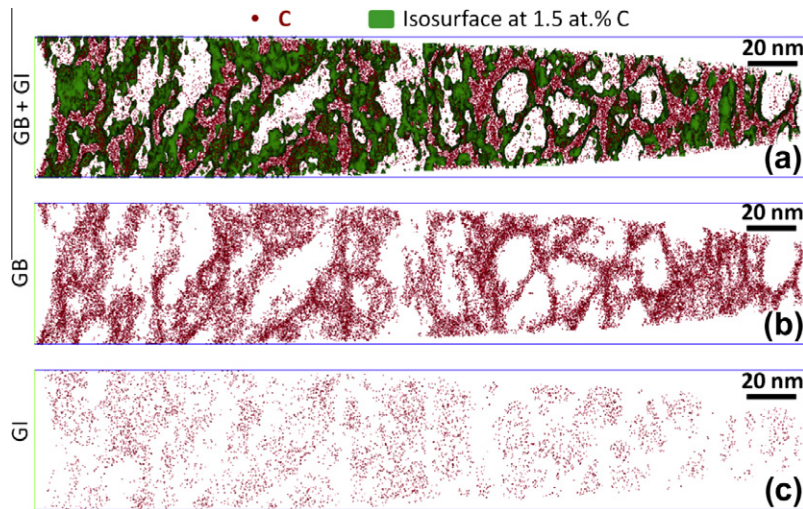


Fig. 1. Example of carbon atom (red dots) maps of a nanocrystalline Fe–C alloy (alloy B annealed at 573 K for 1 h). The analyzed volume is divided into subvolumes for analysis of the carbon concentration at grain boundaries and in grain interiors. The subvolumes are separated by isoconcentration surfaces with  $x = 1.5$  at.% C. (a) Total volume with isoconcentration surfaces in green, (b) grain boundaries and (c) grain interiors. (For interpretation of the references to color in this figure legend, the reader is referred to the web version of this article.)

own specified mass spectrum was analyzed. Moreover, the carbon concentration in grain interiors was determined with high statistics due to the large analyzed volume, as shown in Fig. 1c.

The carbon excess at grain boundaries was measured by means of direct counting of carbon atoms per grain boundary area, as described in previous work [38,39]. As the apparent carbon-enriched zone at grain boundaries is wider than the true width of a grain boundary, an analyzed volume with 4 nm width in the normal direction to the grain boundary was chosen to evaluate the grain boundary excess of carbon.

### 3. Results

#### 3.1. Characterization of the microstructure

XRD patterns of the ball-milled powders with different  $x_{tot}$  are shown in Fig. 2. For alloys A–F, only the peaks

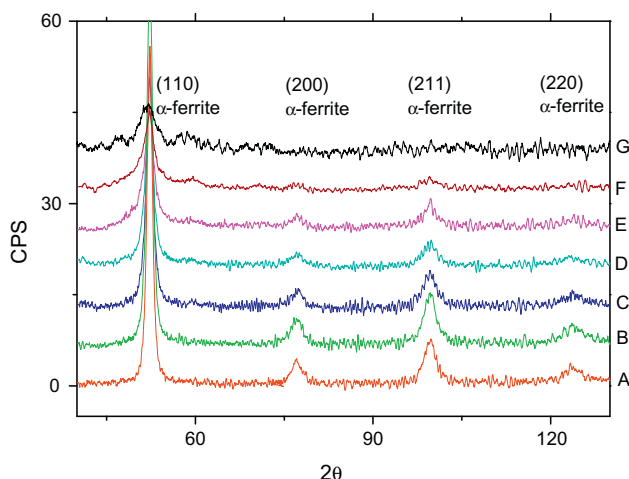


Fig. 2. XRD patterns of the ball-milled Fe–C powders.

corresponding to ferrite can be observed, despite the fact that  $x_{tot}$  is much higher than the equilibrium solubility of carbon in  $\alpha$ -ferrite at room temperature. When  $x_{tot}$  reaches the highest value of 19.40 at.% C (alloy G), only one rather broad peak is detected. In addition, the profile of this peak shows strong diffuse background scattering, indicating a large fraction of amorphous structure formed in this alloy with the highest carbon concentration, which is in agreement with results of Ogasawara et al. [40].

As  $x_{tot}$  increases, broadening of the Bragg peaks becomes more and more significant. Broadening of Bragg peaks can be caused by a decreasing grain size and increasing microstrain [41]. According to Ref. [42], dislocations are the main sources of microstrains in ball-milled iron powders. In order to separate contributions from grain size and dislocations to the broadening of Bragg peaks of ferrite, XLPA was performed on the measured XRD line profiles.

Fig. 3 shows a pattern of alloy C fitted by eCMWP, revealing a perfect fitting by the applied analysis. Unfortunately, this fitting procedure could not give satisfactory solutions in alloys with high carbon concentrations (E, F and G) due to the strong scattered background of the corresponding XRD patterns. Table 2 shows the results of XLPA and eCMWP for the alloys A–D. It can be seen that with increasing  $x_{tot}$ , the grain size of the ball-milled powders decreases continuously. The dislocation densities of these powders are of the order of  $10^{16} \text{ m}^{-2}$ , which corresponds to the saturation value in iron [16].

Typical TEM micrographs of the ball-milled nanocrystalline Fe–C alloys are shown in Figs. 4–6. For low  $x_{tot}$ , only ferrite can be resolved from the selected-area diffraction pattern (SADP), see Fig. 4a. Fig. 4b–d are dark-field images of alloy B corresponding to (110), (200) and (211) Bragg reflections of ferrite. As can be seen, volume fractions of grains with different crystal orientations are



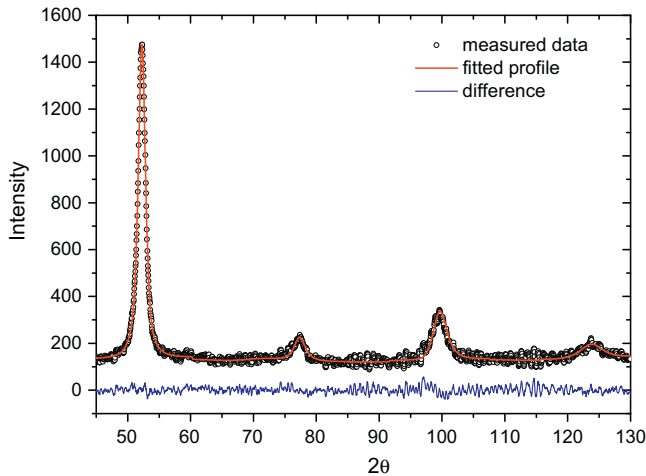


Fig. 3. Result of XLPA with eCMWP fitting for alloy C. Open circles, red line and blue line are measured data, fitted profile and the difference between the measured and fitted data, respectively. (For interpretation of the references to color in this figure legend, the reader is referred to the web version of this article.)

quite similar, showing the typical characteristic of untextured structures. In the case of high  $x_{tot}$ , besides ferrite, two Bragg reflections of  $\text{Fe}_3\text{C}$ , i.e. (210) and (221), which cannot be distinguished in XRD patterns, are visible in the SADP, see Fig. 5a. As for alloy B, volume fractions of ferrite grains in alloy E are equivalent with respect to different crystal orientations. When  $x_{tot}$  reaches the highest value (alloy G), the microstructure exhibits amorphous characteristics in some parts (see Fig. 6a and c), while in some other parts a diffraction pattern contains both the diffraction rings of ferrite and  $\text{Fe}_3\text{C}$ , see Fig. 6b. In Fig. 6a the diffraction ring shows a uniform contrast, indicating that it stems from amorphous regions. Some dark regions (marked by arrows) are observed in the microstructure, revealing that there are at least some crystallites embedded in an amorphous structure. This is also what Fig. 6c suggests. The diffraction ring in Fig. 6b shows a grainy structure; this resembles a Debye–Scherrer ring from randomly oriented crystalline grains. In Fig. 6b both the diffraction rings of ferrite and  $\text{Fe}_3\text{C}$  are detected.

According to the above TEM results alloys A–D consist of single ferrite phase, alloys E and F of ferrite +  $\text{Fe}_3\text{C}$ , C, and alloy G of amorphous regions + ferrite +  $\text{Fe}_3\text{C}$ . These observations are in agreement with the results from Hidaka et al. [43], who showed that  $\text{Fe}_3\text{C}$  will be present in the final microstructures when the carbon concentration of the ball-milled Fe–C alloys is higher than 2 wt.% (8.70 at.%).

Statistical analyses on the TEM dark-field images of the ball-milled powders indicate that the grain size of the ball-milled powders follows a log-normal distribution, see Fig. 7. Therefore, the area weight of the grain size distribution is taken as the mean value, which can also be expressed as  $d_{area}^{TEM} = m \exp(2.5\sigma^2)$ . A typical result of XLPA and TEM analysis on the distribution of the grain size of ferrite is shown in Fig. 7 for alloy C. The results for all alloys reveal that  $d_{area}^{XLPA}$  is always slightly smaller than  $d_{area}^{TEM}$ . This phenomenon is often observed in nanocrystalline materials prepared by severe plastic deformation (SPD), since their microstructures consist of subgrains or dislocation cells that cause additional X-ray scattering [36]. Combining the analyses on some annealed samples (not shown in this work), the difference between  $d_{area}^{TEM}$  and  $d_{area}^{XLPA}$  is within the range of 1–2 nm. Apparently,  $d_{area}^{TEM}$  is more reliable in determining the mean grain size ( $d_{mean}$ ) of the nanocrystalline ferrite. If the average deviation between  $d_{area}^{XLPA}$  and  $d_{area}^{TEM}$  is chosen as 1.5 nm, a relationship of  $d_{mean} = d_{area}^{TEM} = d_{area}^{XLPA} + 1.5 \text{ nm}$  is obtained.

### 3.2. Partitioning of carbon between grain boundaries and grain interior

XRD measurements of the lattice parameters of the ferrite were used to obtain the carbon concentration within the grain interiors of ferrite ( $x_{gi}$ ) ranging from 0.4 to 0.9 at.% as presented in Table 3. From these values the excess carbon at grain boundaries  $\Gamma$  was calculated via Eq. (4) using the total carbon concentration,  $x_{tot}$ , and the mean grain size,  $d_{mean}$ , (cf. Table 2). In Ref. [38] the excess carbon was overestimated because the unalloyed graphite was not separated from the Fe–C alloy powders yielding larger values of  $x_{tot}$ . The average value of  $\Gamma$  for alloys C

Table 2

Results obtained by X-ray line profile analysis (XLPA) via eCMWP fitting [32–34] and by fitting TEM dark-field images:  $\rho$  is the dislocation density,  $m$  the median of grain size,  $\sigma$  its variance and the corresponding grain diameter  $d_{area} = m \exp(2.5\sigma^2)$  [36].  $d_{mean}$  is either  $d_{area}^{TEM}$  (if available) or  $d_{area}^{XLPA} + 1.5 \text{ nm}$  (cf. text).

	A	B	C	D	E	F	G
$x_{tot}$ (at.%)	0.93	1.77	3.27	6.19	13.34	14.21	19.4
$m^{XLPA}$ (nm)	7.04	7.37	5.17	3.40			
$\sigma^{XLPA}$	0.52	0.38	0.45	0.48			
$d_{area}^{XLPA}$ (nm)	13.7	10.7	8.5	6.0			
$\rho$ ( $10^{16} \text{ m}^{-2}$ )	$3.2 \pm 0.4$	$4.0 \pm 0.3$	$1.9 \pm 0.2$	$2.2 \pm 0.4$			
$m^{TEM}$ (nm)		8.29	7.92		4.64	4.9	
$\sigma^{TEM}$		0.36	0.35		0.28	0.28	
$d_{area}^{TEM}$ (nm)		11.4	10.8		5.6	6.0	
$d_{mean}$ (nm)	14.2	11.4	10.8	7.5	5.6	6.0	

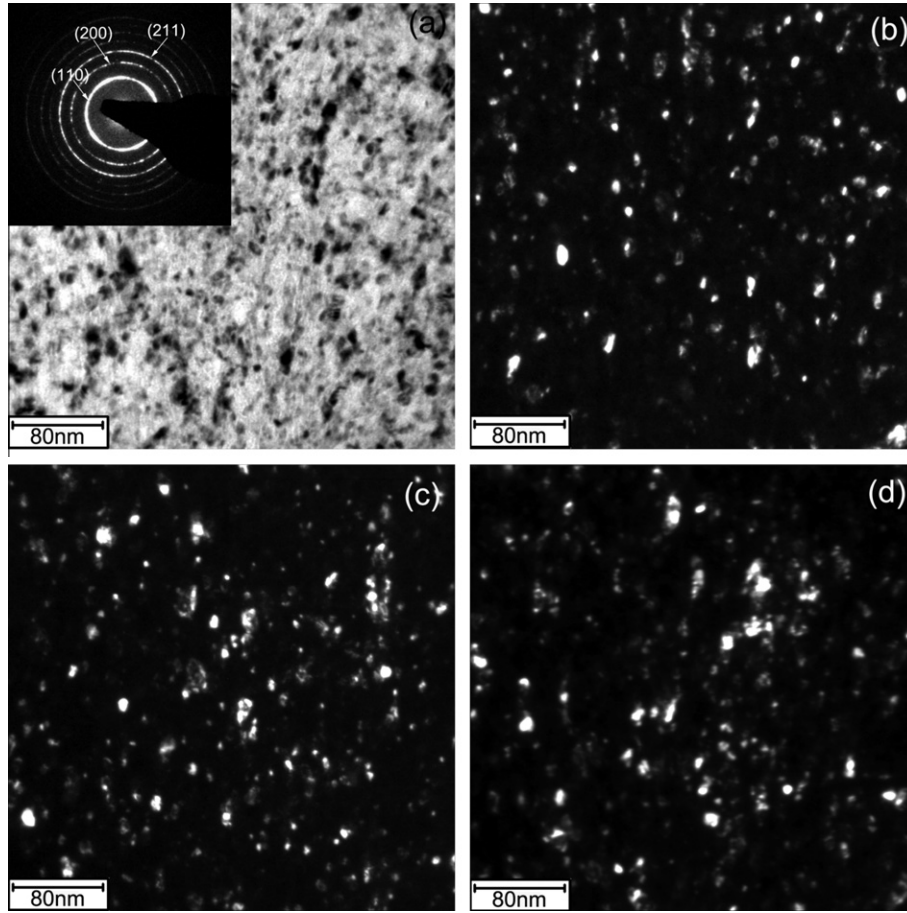


Fig. 4. TEM micrographs of alloy B: (a) bright-field image with diffraction pattern; (b and c) dark-field images corresponding to reflections (110), (200) and (211) of ferrite.

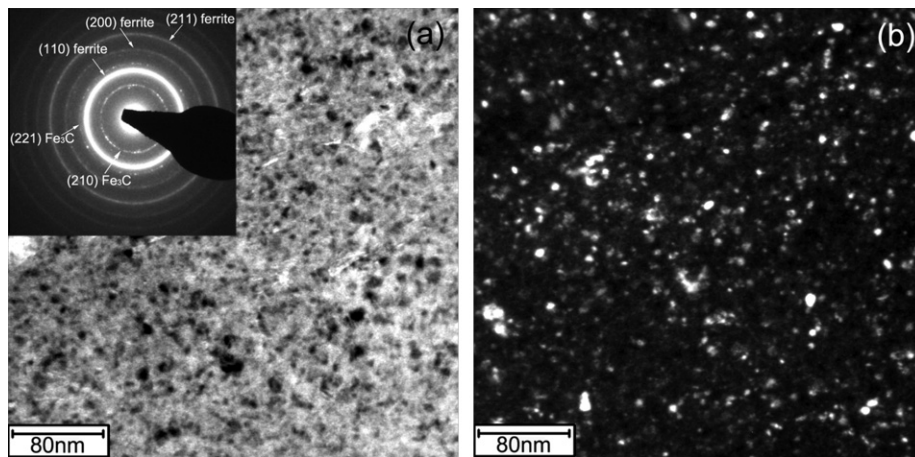


Fig. 5. TEM micrographs of alloy E: (a) bright-field image with diffraction pattern; (b) dark-field image corresponding to Bragg reflections (110) of ferrite.

and D corresponds to  $1.4 \pm 0.1 \times 10^{-5}$  mole-C m $^{-2}$  in the ball-milled state, whereas alloys with relatively low  $x_{tot}$  (alloys A and B) yield lower values for  $\Gamma$ , indicating that the boundaries are not saturated with carbon. Annealing of alloy B at 573 K for 1 h raises the excess carbon from a value of  $0.7 \pm 0.1 \times 10^{-5}$  to  $1.2 \pm 0.1 \times 10^{-5}$  mole-

C m $^{-2}$ , whereas the same annealing treatment of alloy C causes no change within the limits of error (cf. Table 3).

In order to analyze the segregation of carbon in the grain boundaries of ferrite directly, APT measurements were performed. Fig. 8 shows 2-D atom maps of alloy B in both as-milled (Fig. 8a) and as-annealed (Fig. 8c) states

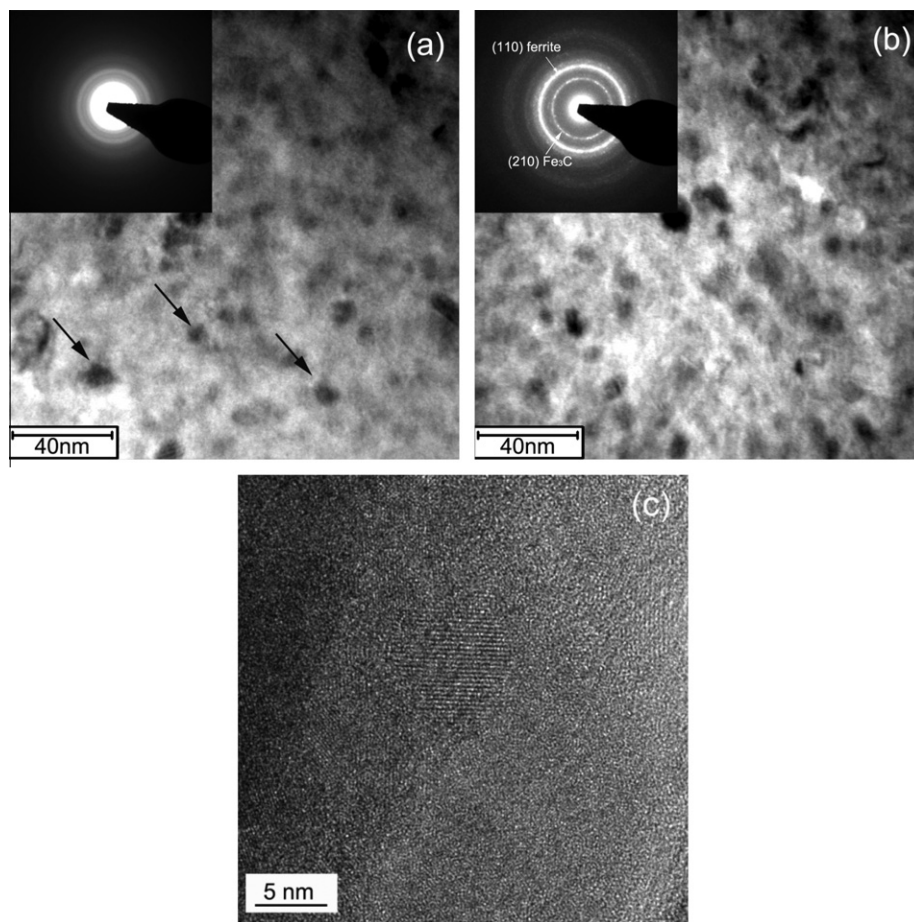


Fig. 6. TEM micrographs of alloy G: (a and b) bright-field images, and (c) a high-resolution image. Marked by arrows in (a) are dark regions revealing that there are at least some crystallites embedded in an amorphous structure.

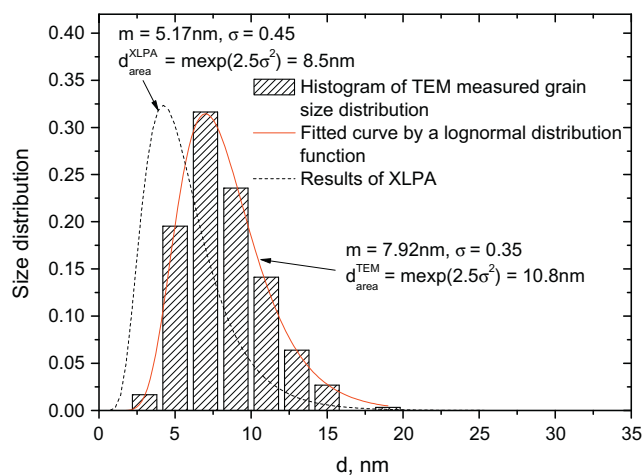


Fig. 7. Grain size distributions of ferrite of the as-milled alloy C. The grain size is measured from the dark-field images with orientations of (110), (200) and (211) of ferrite. The measured grain size distributions are shown in the histograms, which are then fitted by a log-normal distribution function with  $\sigma^2$  the variance and  $m$  the median. The grain size distribution obtained by XLPAs is also plotted for a comparison with TEM results.

and alloy C in the as-milled state (Fig. 8b). As the grain size measured by TEM is  $\sim 10$  nm for the two alloys, the slice

thickness of the 2-D atom maps was chosen to be 10 nm, which gives a better visualization of grain boundaries and avoids their overlap. It can be seen that carbon segregates to grain boundaries in all cases. 1-D carbon concentration profiles of the three states for the selected regions are displayed in Fig. 9. In the ball-milled state, the carbon concentration in grain boundaries of alloy C is apparently higher than that of alloy B. While after annealing treatment at 573 K for 1 h where a precipitation of  $\text{Fe}_3\text{C}$  is not observed, the peak value of carbon concentration in grain boundaries of the annealed alloy B increases and is comparable to that of alloy C. Also, it can be seen that upon annealing the carbon concentration in the valleys of the 1-D carbon profiles of alloy B decreases, which indicates that carbon atoms are moved from grain interiors to grain boundaries during annealing at 573 K for 1 h.

Besides iron and carbon, the elements zirconium and oxygen were also detected during APT. The latter two elements were within the same small regions of about 10 nm in diameter. These features seemed to be debris from the  $\text{ZrO}_2$  balls used in the milling process. As zirconia is a very stable oxide it will not dissolve within the ferrite and, therefore, does not affect carbon activity and carbon partitioning between grains and grain boundaries.



Table 3

Carbon concentration within the grains,  $c_{gi}$ , and excess carbon at grain boundaries  $\Gamma$  of the ferrite (alloys A–D). The first two rows of data are determined by means of the measured lattice parameters of ferrite and Eq. (4). The last two rows are values determined directly by APT.

Alloys	A	B	B (573 K)	C	C (573 K)	D
$x_{gi}$ (XRD), at.% C	$0.6 \pm 0.2$	$0.5 \pm 0.2$	$0.4 \pm 0.2$	$0.9 \pm 0.2$	$0.6 \pm 0.2$	$0.9 \pm 0.2$
$\Gamma$ (XRD), mole-C m <sup>-2</sup>	$0.3 \pm 0.1 \times 10^{-5}$	$0.7 \pm 0.1 \times 10^{-5}$	$1.2 \pm 0.1 \times 10^{-5}$	$1.3 \pm 0.1 \times 10^{-5}$	$1.4 \pm 0.1 \times 10^{-5}$	$1.5 \pm 0.1 \times 10^{-5}$
$x_{gi}$ (APT), at.% C		$0.45 \pm 0.006$	$0.35 \pm 0.013$	$0.35 \pm 0.004$		
$\Gamma$ (APT), mole-C m <sup>-2</sup>		$0.78 \pm 0.27 \times 10^{-5}$	$1.22 \pm 0.20 \times 10^{-5}$	$1.37 \pm 0.13 \times 10^{-5}$		

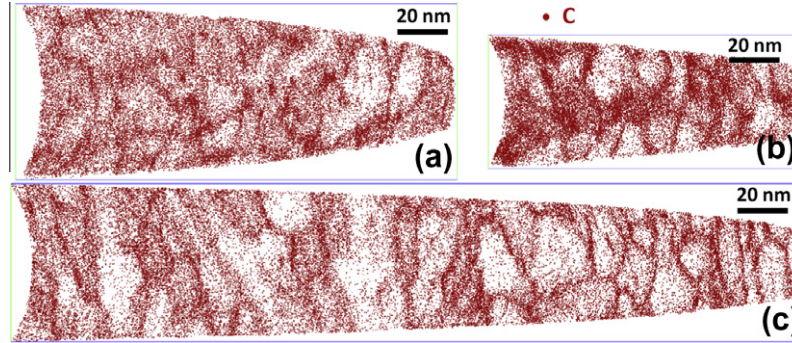


Fig. 8. 2-D (10 nm in thickness) carbon atom maps of (a) alloy B, (b) alloy C and (c) alloy B in the as-annealed (573 K for 1 h) state. All detected carbon atoms are shown.

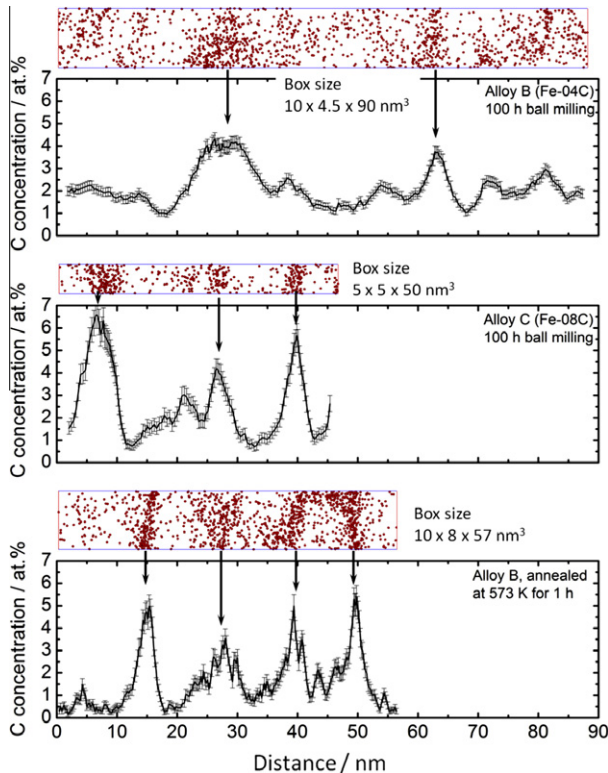


Fig. 9. Carbon atom maps of the selected regions and the corresponding 1-D carbon concentration profiles (fixed sample counts 2000 atoms per step) for alloy B in the ball-milled state (top), alloy C in the ball-milled state (middle), and alloy B in the annealed state (573 K for 1 h) (bottom). The arrows mark concentration peaks at grain boundaries.

The results for  $x_{gi}$  and  $\Gamma_{gb}$  of these three alloys determined by APT are listed in Table 3. It can be seen that

Table 4

Changes in the grain sizes of the nanocrystalline ferrite after annealing treatment in vacuum at 573 K for 1 h.

Alloys	A	B	C	D
$d_{mean}$ (ball-milled state), nm	14.2	11.4	10.8	7.5
$d_{mean}$ (573 K), nm	28.5	19	11.3	8

in the ball-milled state  $x_{gi}$  of alloy B is slightly higher than that of alloy C, while its  $\Gamma$  is apparently lower than that of alloy C. Upon annealing alloy B at 573 K for 1 h, its  $x_{gi}$  decreases to  $0.35 \pm 0.013$  at.%, while  $\Gamma$  increases to  $1.22 \pm 0.20 \times 10^{-5}$  mole-C m<sup>-2</sup>, values equivalent to those of alloy C. As shown in Table 3, the values of  $x_{gi}$  and  $\Gamma$  are consistent with those obtained from XRD analyses. The small deviations for the values of  $x_{gi}$  derived by the XRD method can be ascribed to the above-mentioned uncertainties in evaluating the lattice parameters.

For alloys with low carbon content (alloys A and B) the XRD and APT results show that the grain boundaries were not saturated by carbon after ball milling at room temperature. This saturation occurred during annealing at 573 K and it was accompanied by pronounced grain coarsening (see Table 4). For alloy C the excess carbon at the grain boundaries did not change within the limits of error and after annealing at 573 K and grain growth was negligible. Plotting the values of  $d_{mean}$  after annealing vs. the total carbon concentration,  $x_{tot}$ , as in Fig. 10, shows that for the single ferrite alloys (alloys A–D)  $d_{mean}$  decreases continuously with increasing  $x_{tot}$ , while for the alloys consisting of ferrite and Fe<sub>3</sub>C (alloys E and F),  $d_{mean}$  reaches a lower limit of  $\sim 6$  nm.



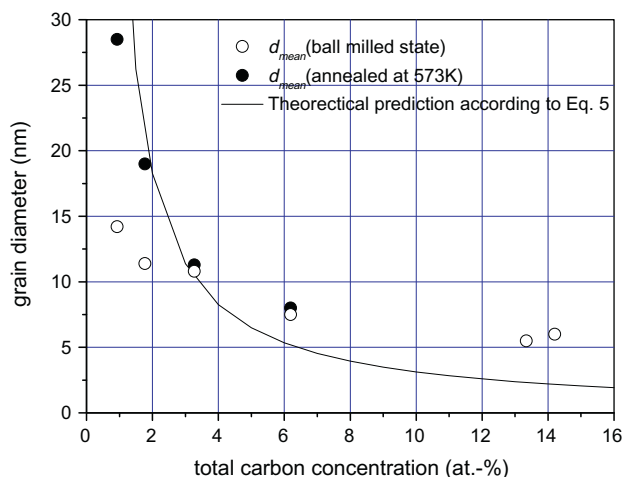


Fig. 10. Evolution of the average grain diameter,  $d_{mean}$  (Tables 2, 4 and text), as a function of the total carbon concentration,  $x_{tot}$ . Experimental values and prediction of Eq. (5) (line drawn with independently determined values of  $x_{gi}^0 = 0.35$  at.-% C and  $\Gamma_{sat} = 1.3 \times 10^{-5}$  mole-C m $^{-2}$ ).

Table 5

Grain size of alloy B after annealing at the given temperature for 1 h in high vacuum ( $10^{-3}$  Pa). The values at the highest temperatures 623, 673 and 873 K were determined by TEM and the ones for the lower temperatures at 423, 473 and 573 K were obtained from X-ray line profile analysis and corrected (cf. text) with respect to TEM values.

Temperature (K)	423	473	573	623	673	873
Grain size (nm)	14	16.2	19.1	20.3	21.6	36.2

### 3.3. Temperature dependence of grain size for the Fe–1.77 at.-% C alloy (alloy B)

Alloy B (1.77 at.-% C) was annealed in a furnace at various temperatures for 1 h under high vacuum ( $\sim 10^{-3}$  Pa) and cooled down to room temperature within the furnace. Afterwards the grain size was determined by XLPD and TEM from dark-field images. The obtained results are compiled in Table 5.

## 4. Discussion

### 4.1. Carbon distribution in Fe–C samples produced by severe plastic deformation

SPD of iron alloys with low carbon content by ball milling always led to nanocrystalline ferrite independent of the starting materials whether these are iron and graphite as in the present study or pearlitic steel as in Ref. [25]. SPD of pearlitic steel by cold wire drawing up to total strains of 6 only caused a partial dissolution of the cementite lamellae. However, in all cases the ferrite lamellae were supersaturated with carbon with concentrations of  $\sim 0.5$  at.-%. In the present study it was shown by both XRD and APT that this concentration is independent both of the grain size and total carbon concentration. This is in agreement with the

requirements of thermodynamic stabilization of the nanostructured alloys as described in the Introduction and in Refs. [4,8,9]. Another requirement for using Eqs. (2) and (5) is a state of solute saturation of grain boundaries. This was proven directly by APT or indirectly by XRD for the high-carbon alloys after ball milling (cf. Table 3). It was shown that metastable equilibrium has not been attained yet in alloys A and B for the ball-milling conditions used in this study, and annealing was necessary to reach the equilibrium values of  $x_{gi}$  and  $\Gamma_{sat}$ .

The excess carbon at saturation  $\Gamma_{sat}$  determined in this study is  $1.3 \pm 0.1 \times 10^{-5}$  mole-C m $^{-2}$  which is about half of a monolayer of the (100) plane of  $\alpha$ -iron ( $2.0 \times 10^{-5}$  mole-Fe m $^{-2}$ ) and close to the carbon density in the (100) plane of cementite Fe $_3$ C ( $1.5 \times 10^{-5}$  mole-C m $^{-2}$ ). It is interesting to note that a similar value of  $\Gamma_{sat}$  was determined for the Ni–P system which has an equilibrium phase Ni $_3$ P [6,17] with the same composition as Fe $_3$ C. In both nanocrystalline alloys Fe–C and Ni–P the given values for  $\Gamma$  are averages over 5–15 boundaries in one sample with a standard deviation of  $< 0.1 \times 10^{-5}$  mole-C m $^{-2}$ . Thus the random distribution of grain orientation (cf. Fig. 4) and orientation of grain boundary planes seemed not to have an effect on the saturated excess carbon despite the expected differences in grain boundary structures. This experimental result may be interpreted as resulting from a 2-D compound formation, where the gain in chemical energy is much larger than the elastic energy for the required small positional changes of the grain boundary atoms to accommodate the 2-D compound. One may also call this a heterogeneous precipitation of a 2-D phase at grain boundaries.

### 4.2. Grain size as a function of total solute content

It has been shown in the previous section that the carbon concentration within the grain interior,  $x_{gi}$ , and the excess carbon,  $\Gamma$ , at the grain boundaries reach values of  $x_{gi}^0$  and  $\Gamma_{sat}$  which are independent of grain size  $d$ . Thus Eq. (5) can be applied as shown in Fig. 10. It is shown that there are large deviations between  $d_{mean}$  in the ball-milled state and the theoretical prediction according to Eq. (5). However, after annealing at 573 K, where a saturation of carbon at the grain boundaries occurs,  $d_{mean}$  at low values of the total carbon content increase significantly. There is a good agreement between the theoretical prediction and experimental values of  $x_{tot}$  and  $d_{mean}$  at low values of the total carbon content. It should be noted that the line shown in Fig. 10 was calculated without a fitting parameter but by using independently determined values of  $x_{gi}^0$  and  $\Gamma_{sat}$ . The same procedure was applied successfully to the nanocrystalline Ni–P system [6,17].

A continuous decrease in the grain size of nanocrystalline alloys with increasing solute content has been observed in many nanocrystalline alloy systems, e.g. Ni–P [6,17], Ni–W [22], Fe–N [44], Pd–Zr [20], Ni–O [45] and as well as by others in the Fe–C system [30]. There are essentially two

competing explanations for this phenomenon, namely a thermodynamic approach and a kinetic approach. The thermodynamic approach attributes the reduction of grain size by increasing solute content to the achievement of a metastable equilibrium in a nanocrystalline alloy system as discussed before. For a comparison of the results obtained in the studies mentioned before, Eq. (5) is rearranged as:

$$\frac{1}{d} = \frac{c_{tot}}{3\Gamma_{sat}} - \frac{c_{gi}^0}{3\Gamma_{sat}}. \quad (6)$$

Thus, plots of the inverse grain size vs. total solute concentration should yield straight lines of slope  $1/(3\Gamma_{sat})$  and intercept  $c_{tot}/(3\Gamma_{sat})$ . Corresponding plots of the results of the present study and for nanocrystalline Fe–N [44], Fe–C [30], Ni–P [6,17] and Ni–O [45] are presented in Fig. 11. In all cases the data at low concentrations can be described by straight lines. For the Ni–P system the line is obtained without a fitting parameter [6] and describes the grain size data well over the entire concentration range. The grain diameter determined by Takaki et al. [16] for Fe–C agrees with the data of the present study, and therefore can be described for low carbon content by Eq. (6) and by the values of  $c_{tot}$  and  $\Gamma_{sat}$  determined in this work too. Aufrecht et al. [44] measured grain diameters of nanocrystalline Fe–N by XRD and as shown in Fig. 11a the results can be fitted to a straight line over the entire concentration range with the same slope as for the Fe–C system. Thus it is concluded that nitrogen in iron has the same excess at grain boundaries after saturation. However, the intercept with the  $c_{tot}$ -axis, i.e. the nitrogen concentration within the grains, is larger. The large concentration  $c_{gi}$  of nitrogen is consistent with the rather large microstrain of  $\sim 0.01$  measured in nanocrystalline nitrogen alloys [44]. In both cases, i.e. nitrogen and carbon, the solute concentration within the grains is much larger than the terminal solubility. The same plot as for Fe–C and Fe–N is shown for the system Ni–O in Fig. 11b. In this system the grain sizes were larger because they were obtained by annealing at 673 K [45]. Moreover, the available data do not fall on a straight line, but a line through the two low-concentration data yields an excess oxygen of  $\Gamma = 1.7 \times 10^{-5}$  mole-O m $^{-2}$  which is close to the oxygen density in the (100)-plane of NiO. Deviations of experimental values from Eq. (6) that occur for Fe–C and Ni–O at higher solute concentrations will be discussed in the following section.

In contrast to the previous thermodynamic interpretation it was suggested for the Fe–N and Fe–C systems, both processed by ball milling, that purely kinetic effects of solute addition should be responsible for the grain refinement [16,44]. In the Fe–N system Aufrecht et al. [44] proposed that the addition of nitrogen immobilizes the grain boundaries formed upon ball milling, which hinders further dynamic recrystallization of the nanostructure and leads to grain refinement. Takaki et al. [16] suggest that in ball-milled Fe–C powders the interaction of carbon with dislocations restricts the mobility of dislocations and

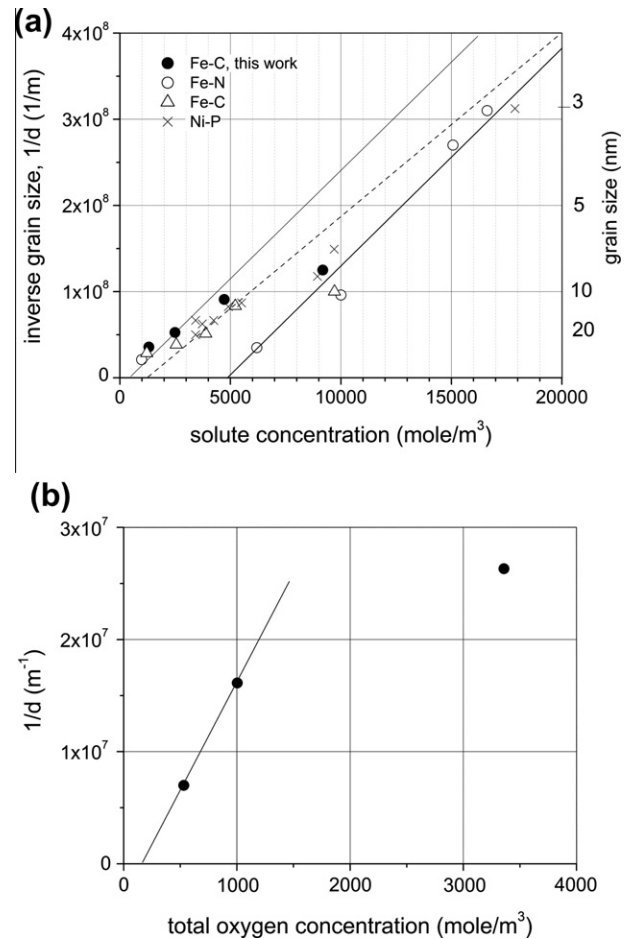


Fig. 11. (a) Following Eq. (6) the inverse grain size is plotted vs. total solute concentration for ball-milled Fe–C (this study, filled circles) and Fe–N [44] (open circles). For comparison, results for Fe–C measured by Takaki et al. [29] (triangles) and for Ni–P [17] (crosses) are presented. The slope of the straight line for carbon corresponds to an excess carbon of  $\Gamma_{gb}^{sat} = 1.3 \times 10^{-5}$  mole-C m $^{-2}$ . According to Eq. (4) the intercept with the abscissa corresponds to the solute concentration within the grains, which is  $x_{gi} = 0.35$  at.% C ( $c_{gi} = 500$  mol-C m $^{-3}$ ) as determined by APT. No APT data are available for nitrogen, and therefore the same value of  $\Gamma_{gb}^{sat}$ , or the slope of the straight line respectively, was chosen as for carbon. For Ni–P both  $\Gamma_{gb}^{sat}$  and  $x_{gi}$  are known, yielding the dashed straight line in agreement with experimental data. (b) Same plot as in (a) but for Ni–O. The straight line through the first two data points corresponds to an excess oxygen of  $\Gamma = 1.7 \times 10^{-5}$  mole-O m $^{-2}$ .

therefore suppresses dynamic recovery. No attempt was made for the two kinetic interpretations to relate the obtained grain sizes to the total solute content.

#### 4.3. Attainment of a metastable equilibrium for nanocrystalline alloys

In a rigorous treatment of the thermodynamics of nanostructures [4,5] Weissmüller has shown that at constant temperature and pressure a metastable equilibrium is reached in closed systems if the grain boundary energy is zero ( $\gamma = 0$ ). Any positive or negative change of the grain size then drives the system back to equilibrium. As the

condition  $\gamma = 0$  corresponds to zero driving force for grain growth, the retarded or missing grain coarsening of nanocrystalline alloys is interpreted as evidence for metastable equilibrium.

For saturated grain boundaries Weissmüller derived Eq. (2) which for  $\gamma = 0$  predicts a definite solute concentration  $x_{gi}$  within the grains. This concentration should be independent of grain size and the total solute content leading to Eq. (6). Thus the agreement with many experimental data as discussed in the previous section could be considered as another piece of evidence for the attainment of metastable equilibrium. The conditions for this equilibrium were also derived in Refs. [8,9] based on Eq. (1) and in a general context of solute–defect interaction. In Appendix A the relation between Eqs. (1) and (2) is discussed.

In the following we will apply Eq. (2) to the experimental data of this work which is very appropriate as the quantities in Eq. (2) were either measured in this work or are available in the literature. For  $\gamma_o = 0.79 \text{ J m}^{-2}$  (grain boundary energy of pure iron) [46],  $x_{gi} = 0.0035$  ( $x_{gi} = 0.35 \text{ at.}\%$ ), and  $\Gamma_{sat} = 1.3 \times 10^{-5} \text{ mole m}^{-2}$  a rather large value of the segregation enthalpy  $\Delta H_{seg} = 74 \text{ kJ mole-C}^{-1}$  would be required, in order to attain a zero grain boundary energy at 295 K. This value is larger than the average experimental value of about  $55 \text{ kJ mole-C}^{-1}$  for a variety of tilt boundaries determined by Auger electron spectroscopy in the Fe–C system [47]. However, the published experimental values of  $\Delta H_{seg}$  vary over a large range between 38 and  $80 \text{ kJ mole-C}^{-1}$  [47] and were determined at higher temperatures than 295 K, different carbon concentrations and larger grain sizes. Taking also the error bars of the values inserted in Eq. (2) into account the agreement between thermodynamic prediction and experiment is considered to be good for the nanocrystalline Fe–C system at low total carbon concentrations. For the nanocrystalline Fe–N results shown in Fig. 11a the values  $x_{gi} = 0.035$ , and  $\Gamma_{sat} = 1.3 \times 10^{-5} \text{ mol m}^{-2}$  may be appropriate, yielding  $\Delta H_{seg} = 68 \text{ kJ mol-N}^{-1}$  which agrees with the experimental results of  $\Delta H_{seg} = 88 \pm 12 \text{ kJ mol-N}^{-1}$  [48]. As for carbon, the nitrogen concentration within the grains is orders of magnitude above the terminal solubility in  $\alpha$ -iron [49]. However, this solubility of nitrogen in equilibrium with  $\text{Fe}_4\text{N}$  at 300 K [49] is much larger than the corresponding value for carbon in equilibrium with  $\text{Fe}_3\text{C}$  [50], which supports the values for  $x_{gi}$  determined in this study.

#### 4.4. Grain size as a function of temperature

It is assumed that for the alloys with a low carbon content the grain size obtained after ball milling does not correspond to the one given in Eq. (5), because the equilibrium between carbon within the grains and within grain boundaries has not yet been attained. This is supported by the fact that the excess carbon at the grain boundaries is lower after preparation than the saturation values for alloy B reached at 573 K (see Table 3). If the grain size after ball milling is smaller than the one given by Eq. (5), grain

growth and redistribution of carbon atoms will occur upon annealing treatment, leading to equilibrium, which requires sufficient carbon and grain boundary mobility.

According to the previous discussion, both Eqs. (2) and (5) with  $\gamma = 0$  have to be fulfilled for equilibrium. Under these conditions we can eliminate  $x_{gi} = c_{gi}V_{Fe}$  ( $c_{gi}$  is in  $\text{mole m}^{-3}$ ,  $V_{Fe}$  = molar volume of Fe) from both equations, replace  $c_{tot}$  by  $x_{tot} = c_{tot}V_{Fe}$  and obtain an implicit relation between grain diameter and temperature:

$$\ln \left[ x_{tot} - \frac{3\Gamma_{sat}V_{Fe}}{d} \right] = \frac{\frac{\gamma_o}{\Gamma_{sat}} - \Delta H_{seg}}{RT}. \quad (7)$$

Based on this equation, the values of Table 5 are plotted in Fig. 12. The high-temperature values fall on a straight line in agreement with Eq. (7), but the intercept with the ordinate at  $-2.60 \pm 0.16$  is not zero. The latter deviation from Eq. (7) may be due to entropic contributions to the segregation free energy and the grain boundary energy. The intercept and the slope of  $-1700 \pm 100 \text{ K}^{-1}$  were obtained from a linear fit to the points shown in Fig. 12. The low-temperature data deviate remarkably from the linear fit which may be due to not corresponding to equilibrium values. If the values of  $\gamma_o = 0.78 \text{ J m}^{-2}$  and  $\Gamma_{sat} = 1.3 \times 10^{-5} \text{ mole-C m}^{-2}$  are used as before, the slope of the linear fit yields  $\Delta H_{seg} = 45.9 \text{ kJ mole-C}^{-1}$ . This value corresponds remarkably well to the predicted value of  $50.4 \text{ kJ mole-C}^{-1}$  predicted by Lejček and Hofmann [47], and is a little smaller than the average experimental value of  $55 \text{ kJ mole-C}^{-1}$  [47]. It is, however, somewhat smaller when compared to the previous evaluation based on Eq. (2) which gave a larger value of  $74 \text{ kJ mole-C}^{-1}$ .

The increasing grain diameter with increasing temperature can be explained via Eq. (2) as follows: based on the assumption that the quantities  $\gamma_o$ ,  $\Delta H_{seg}$  and  $\Gamma_{sat}$  do not depend strongly on temperature, the remaining term  $RT \ln x_{gi}^o$  has to be independent of temperature as well, if the equilibrium condition  $\gamma = 0$  is to be fulfilled. Thus  $x_{gi}^o$  (or  $c_{gi}^o$ ) have to increase with increasing temperature, which causes an increase in grain size because of Eq. (6), i.e. grain

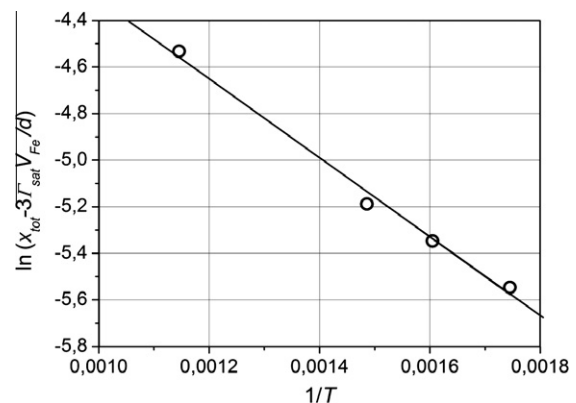


Fig. 12. Plot of the high-temperature values of Table 5 according to Eq. (7). The straight line is a linear fit through the data points yielding a slope of  $-1700 \pm 100$  and an intercept with the ordinate of  $-2.60 \pm 0.16$ .



boundary area has to be annihilated to provide the necessary carbon for the grain interior.

#### 4.5. Grain boundary segregation and the onset of precipitation

Taking the empirical correlation [7] between terminal solubility and segregation tendency into account, it has been shown in Ref. [6] that the reduction in grain boundary energy ( $\gamma_o - \gamma$ ) is only 0.06–0.4 J m<sup>-2</sup> if  $x_{gi}$  in Eq. (2) is not allowed to exceed the terminal solubility. Thus grain boundary energies, having average values of  $\sim 1$  J m<sup>-2</sup>, will become zero only if supersaturation of solutes within the grain interiors is allowed. This conclusion is in agreement with the measured values for carbon in iron obtained by APT in this study. Supersaturation in this case may be possible because of the difficulties in nucleating the equilibrium-phase Fe<sub>3</sub>C. Supersaturation within the grains has also been observed for nanocrystalline Ni–P. By formation of the equilibrium phase Ni<sub>3</sub>P at temperatures above 673 K saturation was reduced and according to Eq. (2) the grain boundary energy became positive again, leading to grain growth.

At higher carbon contents the formation of the equilibrium phase Fe<sub>3</sub>C has been observed in alloys E and F. The corresponding carbon part corresponding to Fe<sub>3</sub>C is not considered in Eq. (6), and therefore deviations from the straight line may occur as for alloy D, although the corresponding small fraction of Fe<sub>3</sub>C particles was not detected in TEM micrographs of this alloy. Here, the question arises as to why not all of the carbon is deposited as excess solute at grain boundaries, reducing the grain size accordingly. One explanation might be that we have not yet reached the metastable equilibrium, simply because the ball-milling time was not sufficiently long for the high carbon content. For grain sizes below the experimental limit of  $\sim 6$  nm, there might be also energy contributions arising from the increasing curvature of the grains or increasing total length of triple lines which counteract any further reduction in grain size. While this might explain the deviations observed for Fe–C and Ni–O in Fig. 11, it then raises the question why it does not occur for Ni–P and Fe–N.

#### 4.6. Formation of Fe<sub>3</sub>C and amorphous structure in the FeC alloys at high carbon contents

When  $x_{tot}$  reaches high values, i.e. in alloys E–G, the formation of nanostructures becomes more complicated due to the formation of the Fe<sub>3</sub>C phase with an amorphous structure. The grain size of these alloys reaches a lower limit and some of the carbon agglomerates as Fe<sub>3</sub>C. If Fe<sub>3</sub>C is severely deformed during ball milling, the deformation-driven amorphization of Fe<sub>3</sub>C would be expected as observed in heavily deformed pearlitic steels [51–53] and Cu–Nb–Ag alloys [54]. A detailed discussion on the deformation-driven amorphization is described elsewhere [54]. In fact, the amorphization of Fe<sub>3</sub>C may also occur in alloys

E and F, whereas the volume fraction of the amorphous structure may be too low to be detected.

## 5. Conclusions

- (1) Single nanocrystalline ferrite structures are observed after ball milling of iron and graphite at low carbon concentrations, whereas at higher concentrations the nanostructures consist of ferrite and Fe<sub>3</sub>C. At the highest carbon content of 19.40 at.% C a mixture of ferrite, Fe<sub>3</sub>C and an amorphous phase is found. The grain size of ferrite decreases with increasing carbon concentration and reaches a lower limit of  $\sim 6$  nm.
- (2) A strong segregation of carbon at grain boundaries of ferrite is observed by APT which saturates during ball milling or after annealing at 573 K with the same excess of  $1.3 \times 10^{-5}$  mole-C m<sup>-2</sup> for all grain boundaries analyzed within one sample and independent of the total carbon content or the grain size, respectively.
- (3) The carbon concentration within the ferrite grains of  $\sim 0.35$  at.% corresponds to a highly supersaturated state or a high chemical potential. Thus the Gibbs adsorption isotherm predicts a large decrease in the grain boundary energy.
- (4) A metastable equilibrium with zero grain boundary energy is attained in the low-carbon alloys as proven by the good agreement of experimental results with (i) the validity of Weissmüller's equation, (ii) the predicted dependence of grain size upon total carbon concentration and (iii) the newly derived temperature dependence of grain size.
- (5) A metastable equilibrium with zero grain boundary energy is not reached for the alloys with a carbon content of  $\geq 6$  at.% C for the given milling conditions, because some of the carbon is consumed by the formation of crystalline or amorphous cementite instead of being deposited at additional and newly formed grain boundaries. Thus the grain size does not decrease below 6 nm.

## Acknowledgements

Support by the Deutsche Forschungsgemeinschaft (KI 230/34-1 and SFB 602 TP B13) is gratefully acknowledged. Y.Z.C. thanks the Alexander von Humboldt Foundation for a Research Fellowship and the Natural Science Foundation of China (Nos. 51101121 and 51125002), the Research Fund of the State Key Laboratory of Solidification Processing (NWPU) (No. 79-TP-2011), and the Fundamental Research Fund of NWPU (No. JC2001134) for his work in NWPU. He is also grateful for fruitful discussions with Professor F. Liu from the Northwestern Polytechnical University, Xi'an.

## Appendix A. Relation between Gibbs' and Weissmüller's equation

In Appendix B of Ref. [8] it was proven in a semiquantitative way that Eq. (2) is a special case of Eq. (1). The reasoning will be repeated here and it will be extended by including the Langmuir–McLean segregation isotherm leading to a quantitative relationship.

In Fig. A1 the grain boundary energy,  $\gamma$ , is plotted vs. the chemical potential of the solute,  $\mu$ . For  $\mu \rightarrow -\infty$  the total concentration as well as the excess become very small, i.e.  $\Gamma \rightarrow 0$  and the curve  $\gamma(\mu)$  starts with zero slope according to Eq. (1). Increasing  $\mu$  finally leads to saturation of grain boundaries with an excess  $\Gamma_{sat}$  and a corresponding constant negative slope of the  $\gamma(\mu)$  curve. Assuming that the turnover from zero to constant slope occurs at  $\mu = \Delta H_{seg}$  (with the standard value of the chemical potential set to  $\mu_A^o = 0$ ), Eq. (2) is expressing the slope of the triangle shown in Fig. A1 by:

$$\Gamma_{sat} = \frac{\gamma_o - \gamma}{\Delta H_{seg} - \mu} = \frac{\gamma_o - \gamma}{\Delta H_{seg} - RT \ln x_{gi}}. \quad (A1)$$

Besides this geometrical derivation a direct integration of Eq. (1) from  $\mu_A = \Delta H_{seg}$  to  $\mu = RT \ln x_{gi}$  with  $\Gamma = \Gamma_{sat}$  yields the same result.

In order to determine the turnover quantitatively the function  $\Gamma(\mu_A)$  has to be known. An analytical expression for this function is derived in the following based on the Langmuir–McLean equation which is presented here in a form given in Ref. [4]:

$$\frac{N_{gb}}{N_{gb}^{sat} - N_{gb}} = \frac{N_{gi}}{N_o} \exp\left(\frac{\Delta H_{seg}}{RT}\right), \quad (A2)$$

where  $N_{gb}$  and  $N_{gi}$  are the number of A atoms in the grain boundaries or in the grain interior, respectively,  $N_{gb}^{sat}$  and  $N_o$  are the number of available lattice sites in the grain boundaries or in the grain interior, respectively. If the density of

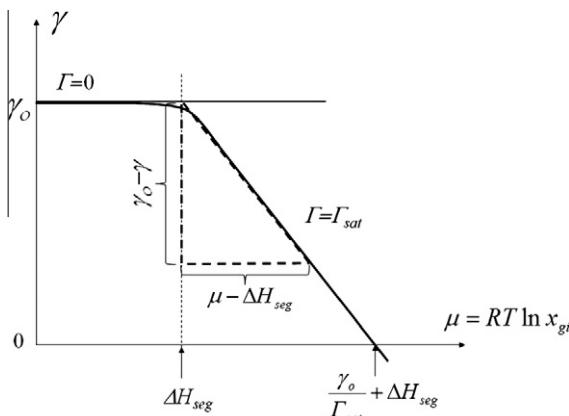


Fig. A1. Schematic presentation of the grain boundary energy  $\gamma$  as a function of the chemical potential  $\mu$  of a segregating solute according to Eq. (1) and saturation of the excess solute  $\Gamma$  at the grain boundary. The dashed triangle is a geometrical presentation of Eq. (2) (cf. text in Appendix A).

these sites, i.e. the latter two numbers per volume is equal, the excess is given by:

$$\Gamma = \frac{N_{gb} - N_{gi}N_{gb}^{sat}/N_o}{A}, \quad (A3)$$

where  $A$  is the total grain boundary area. Inserting  $N_{gb}$  from Eq. (A2) yields

$$\Gamma A = \frac{N_{gb}^{sat}}{N_o \exp(-\Delta H_{seg}/RT)/N_{gi} + 1} - N_{gi}N_{gb}^{sat}/N_o. \quad (A3)$$

For low solute concentrations within the grain interior, the chemical potential is given by:

$$\mu = \mu^o + RT \ln \frac{N_{gi}}{N_o} = \mu^o + RT \ln x_{gi}. \quad (A4)$$

Inserting Eq. (A4) into Eq. (A3) leads to:

$$\Gamma = \frac{N_{gb}^{sat}}{A} \left\{ \frac{1}{\exp[(\mu - \mu^o)/RT] + 1} - \exp[(\mu - \mu^o)/RT] \right\}. \quad (A5)$$

Integrating the Gibbs adsorption isotherm (Eq. (1)) with Eq. (A5) gives:

$$\begin{aligned} \gamma &= \gamma_o - \int_{-\infty}^{\mu} \Gamma d\mu = \gamma_o - RT \int_{-\infty}^{\mu} \Gamma d\left(\frac{\mu - \mu^o}{RT}\right) \\ &= \gamma_o + \frac{N_{gb}^{sat} RT}{A} \left\{ \exp\left(\frac{\mu - \mu^o}{RT}\right) - \ln \left[ 1 + \exp\left(\frac{\Delta H_{seg} + \mu - \mu^o}{RT}\right) \right] \right\}. \end{aligned} \quad (A6)$$

Excess saturation for dilute solutions within the grain interior ( $N_{gi}/N_o \ll 1$ ) corresponds to  $\Gamma_{sat} = N_{gb}^{sat}/A$ . Three limiting cases are derived from Eq. (6):

- $\gamma = \gamma_o$  for  $\mu - \mu^o \rightarrow -\infty$
- $\gamma = \gamma_o + \Gamma_{sat} RT$  for  $\mu - \mu^o \ll \Delta H_{seg}$  which corresponds to a relation derived by Seah [53]
- $\gamma = \gamma_o + \Gamma_{sat}(\Delta H_{seg} + \mu - \mu^o) = \gamma_o + \Gamma_{sat}(\Delta H_{seg} + RT \ln x_{gi})$  for  $\mu - \mu^o \gg \Delta H_{seg}$  which is equivalent to Eq. (2). The corresponding straight line intersects the horizontal line  $\gamma = \gamma_o$  at  $RT \ln x_{gi} = \Delta H_{seg}$  in agreement with the assumption in Ref. [8].

## References

- [1] Gleiter H. Prog Mater Sci 1989;33:223.
- [2] Gibbs JW. Trans Conn Acad, 1876, vol. III, 108–248 and 1878, vol. III, 343. Also in: The Collected Work of J.W. Gibbs, vol. I. New York: Longmans, Green & Co.; 1928. p. 55.
- [3] Krill CE. Private communication. The concept was presented by Rainer Birringer at a workshop on “Metastable Phase Formation in the Solid State”, held 27–31 July 1992, Kloster Irsee.
- [4] Weissmüller J. Nanostruct Mater 1993;3:261.
- [5] Weissmüller J. J Mater Res 1994;9:4.
- [6] Kirchheim R. Acta Mater 2002;50:413.
- [7] Hondros ED, Seah MP, Hofmann S, Lejcek C. In: Cahn RW, Haasen P, editors. Physical metallurgy, vol. 2. Amsterdam: North Holland; 1996. p. 1224.
- [8] Kirchheim R. Acta Mater 2007;55:5129.
- [9] Kirchheim R. Acta Mater 2007;55:5139.

- [10] Kirchheim R. *IJMR (Z Metall)* 2009;100:483.
- [11] Gao ZQ, Fultz B. *Nanostruct Mater* 1994;4:939.
- [12] Hong LB, Bansal C, Fultz B. *Nanostruct Mater* 1994;4:949.
- [13] Abe YR, Johnson WL. In: *Mechanical alloying, materials, science forum*, vols. 88–90. Zurich: TransTech; 1992. p. 513.
- [14] Liu KW, Mücklich F. *Acta Mater* 2001;49:395.
- [15] Mehta SC, Smith DA, Erb U. *Mater Sci Eng A* 1995;204:227.
- [16] Michels A, Krill CE, Ehrhardt H, Birringer R, Wu TD. *Acta Mater* 1999;47:2143.
- [17] Färber B, Cadel E, Menand A, Schmitz G, Kirchheim R. *Acta Mater* 2000;48:789.
- [18] Choi P et al. *Acta Mater* 2005;53:4473.
- [19] Darling KA et al. *Scripta Mater* 2008;59:530.
- [20] Krill CE et al. *Z Metall* 2005;96:1134.
- [21] Koch CC et al. *J Mater Sci* 2008;43:7264.
- [22] Detor AJ, Schuh CA. *Acta Mater* 2007;55:371–9.
- [23] Weissmüller J, Krauss W, et al. *Nanostruct Mater* 1993;1:439.
- [24] Zhang HW, Gopalan R, Mukai T, Hono K. *Scripta Mater* 2005;53:863.
- [25] Ohsaki S, Hono K, Hidaka H, Takaki S. *Scripta Mater* 2005;52:271.
- [26] Miller MK. *Rev Sci Instrum* 2007;78:031101.
- [27] Miller MK, Russell KF. *Surf Interface Anal* 2007;39:262.
- [28] Kelly TF, Miller MK. *Microsc Res Tech* 2006;69:359.
- [29] Miller MK, Forbes RG. *Mater Charact* 2009;60:461.
- [30] Takaki S, Tsuchiyama T, Nakashima K, Hidaka H, Kawasaki K, Futamura Y. *Metals Mater Int* 2004;10:533.
- [31] Sauvage X, Lefebvre W, Genevois C, Ohsaki S, Hono K. *Scripta Mater* 2009;60:1056.
- [32] Balogh L, Ribárik G, Ungár T. *J Appl. Phys* 2006;100:023512.
- [33] Ribárik G, Gubicza J, Ungár T. *Mater Sci Eng* 2004;A387–389:343.
- [34] <http://www.renyi.hu/cmwp/>.
- [35] Chen YZ, Csiszár G, Cizek J, Borchers C, Ungár T, Goto S, et al. *Scripta Mater* 2011;64:390.
- [36] Ungár T, Gubicza J, Ribárik G, Borbely A. *J App Crystallogr* 2001;34:298.
- [37] Fasiska EJ, Wagemblast H. *Trans AIME* 1967;239:1818.
- [38] Chen YZ, Herz A, Kirchheim R. *Mater Sci Forum* 2011;667–669:265.
- [39] Li YJ, Choi P, Goto S, Borchers C, Raabe D, Kirchheim R. *Acta Mater* 2012;60:4005.
- [40] Ogasawara T, Inoue A, Masumoto T. *Mater Sci Forum* 1992;88–90:423.
- [41] Williamson GK, Hall WH. *Acta Metall* 1953;1:22.
- [42] Revesz A, Ungar T, Borbely A, Lendvai J. *Nanostruct Mater* 1996;7:779.
- [43] Hidaka H, Kimura Y, Takaki S. *Tetsu Hagane* 1999;85:52.
- [44] Aufrecht J, Leineweber A, Foct J, Mittemeijer EJ. *Philos Mag* 2008;88:1835.
- [45] Natter H et al. *Scripta Mater* 2001;44:2321.
- [46] Hondros ED. *Proc Roy Soc* 1965;A286:479.
- [47] Lejček P, Hofmann S. *Surf Interface Anal* 2002;33:203.
- [48] Hondros ED. *Metal Sci* 1967;1:36.
- [49] Nacken M, Jargon F. *Arch Eisenh* 1966;37:989.
- [50] Gmelins *Handbuch der anorganischen Chemie. Metallurgie des Eisens*, 4th ed., vol. 1. Weinheim: Verlag Chemie.
- [51] Li YJ, Choi P, Borchers C, Westerkamp S, Goto S, Raabe D, et al. *Acta Mater* 2011;59:3965.
- [52] Languillaume J, Kapelski G, Baudelet B. *Acta Mater* 1997;45:1201.
- [53] Goto S, Kirchheim R, Al-Kassab T, Borchers C. *Trans Nonferrous Met Soc China* 2007;17:1129.
- [54] Raabe D, Ohsaki S, Hono K. *Acta Mater* 2009;57:5254.